Ceramics International 50 (2024) 54778–54790

Contents lists available at ScienceDirect

Ceramics International

journal homepage: www.elsevier.com/locate/ceramint

Understanding the impact of porosity on Li-ion diffusion enhancement in micro-sized silicon particles for advanced batteries

Mahesh B. Naikwade, Pranav K. Katkar *, Sang-Wha Lee **

Department of Chemical and Biological Engineering, Gachon University, 1342 Seongnam-daero, Seongnam-si, 13120, Republic of Korea

ARTICLE INFO

Handling Editor: Dr P. Vincenzini

Keywords:
Micro-sized porous silicon
Metal-assisted chemical etching method
Li-ion diffusion
Energy storage mechanism
Porosity
Battery

ABSTRACT

Lithium-ion batteries (LIBs) require advanced and practical anode materials, such as porous silicon (PSi), which can meet these expectations due to their rapid Li-ion diffusion rates and structural relaxation. Several studies have focused on the structural design of PSi or its composites to improve Li-ion diffusion; however, no systematic and quantitative evaluations of the impact of porosity on Li-ion diffusion and battery performance have been reported. Therefore, to understand the impact of porosity on Li-ion diffusion, we developed micro-sized porous silicon (m-PSi) particles with various porosities via metal-assisted chemical etching (MACE) method using different concentrations of $AgNO_3$ (0.02–0.08 M). Among the as-prepared samples, m-PSi-0.06 (prepared using 0.06 M $AgNO_3$) with ~70 % porosity achieved a maximum Li-ion diffusion rate of 2.35×10^{-9} cm^2 s^{-1}. This led to a high-rate capability, enhanced Li-ion storage, and better cyclic retention of 61.4 % compared to the non-porous micro-sized Si (m-Si) (5.8 %) sample at a current density of 0.1 A g^{-1}. Furthermore, the optimal porosity of m-PSi-0.06 resulted in an impressive rate capability of 760 mAh g^{-1} at a high current density of 4 A g^{-1} with a recovery rate of 80 %. The improved efficiency of m-PSi-0.06 is attributed to its optimized meso-porosity, which ensures sufficient space for Li-ion storage and shortens the effective transmission path to accelerate Li-ion diffusion. Moreover, the mesopores provide a greater number of active sites for the reversible adsorption of Li ions, thereby improving the capacitive behavior of the anode. In contrast, the highly nanoporous m-PSi-0.08, with a pore diameter of 1–3 nm, impeded Li-ion movement and restricted diffusion. These results reveal that a high nano porosity hinders Li-ion diffusion, whereas an optimal mesoporosity ensures swift diffusion in m-PSi anodes. These insights could guide the design of Si-based anode materials for advanced LIBs.

1. Introduction

Silicon is being recapped in the current research interest as one of the most promising anode candidates for next-generation high-energy lithium-ion batteries (LIBs) owing to its remarkable theoretical capacity (4200 mAh g^{-1}, $Li_{22}Si_5$), natural abundance, and moderate working potential (<0.4 V vs. Li/Li^+) [1–3]. However, the poor Li-ion diffusion kinetics, severe volume expansion (300–400 %) [2], and unstable solid electrolyte interface (SEI) layer formation restrict its commercialization in the battery industry [1,4]. Interestingly, micro-sized porous silicon (m-PSi) has demonstrated a potential ability to relieve the fundamental issues of Si anodes, owing to its enhanced Li-ion diffusion kinetics [5,6], effective volume adjustment during cycling [7], and reduced electrode-electrolyte interface resistance [8]. Additionally, the rapid Li-ion diffusion in m-PSi anodes improves the initial capacity, rate capability, and cyclic stability [9–11] of LIBs. However, controlling the porosity of m-PSi anodes is crucial for optimizing Li-ion diffusion kinetics, which remains a significant challenge [12,13]. Moreover, a high charge-discharge rate is essential for improving battery performance, which is fundamentally governed by Li-ion kinetics, often quantified by the diffusion coefficient of Li ions [14,15]. Hence, controlled and stable Li-ion diffusion within the anodes can elevate their working efficiency by facilitating the formation of a stable SEI layer during cyclic operation [16,17].

Since the first report of Li-ion diffusion in nano-silicon by Ding et al., various kinds of research have been carried out to enhance Li-ion diffusion in Si anodes [18]. Furthermore, Arie et al. prepared Si anodes with fullerene, resulting in a two-orders-of-magnitude increase in Li-ion diffusion compared to pristine Si films [19]. Long et al. improved the Li-ion diffusion by designing p-doped Si anodes, achieved through

* Corresponding author.
** Corresponding author.
E-mail addresses: pra123@gachon.ac.kr (P.K. Katkar), lswha@gachon.ac.kr (S.-W. Lee).

https://doi.org/10.1016/j.ceramint.2024.10.337
Received 20 August 2024; Received in revised form 19 October 2024; Accepted 22 October 2024
Available online 22 October 2024

doping Si nanoparticles with phosphorous [20]. Haiping et al. developed a scalable method to accelerate Li-ion diffusion in m-PSi anodes by coating them with 2,3-dihydroxy naphthalene-derived graphitic carbon [21]. Wang et al. developed a unique polymer, poly(hexaazatrinaphthalene), on a micro-sized Si/C surface. Their simulation study and in-situ analysis demonstrated increased Li-ion mobility, with benzene rings serving as hopping sites for ion transport [22]. However, no studies have systematically and sequentially investigated the effect of porosity on the Li-ion diffusion coefficient (D_{Li+}) in m-PSi anodes and its implications for cycle performance. Our optimization study, conducted using the MACE process, is necessary to understand the complex relationship between Li diffusion kinetics and porosity, which is crucial for developing advanced PSi anodes.

In this study, we systematically evaluated the effect of variable porosity on Li-ion diffusion and its implications for the cyclic performance of m-PSi anodes. m-PSi samples with varying porosities were prepared using a facile MACE process by adjusting the concentration of Ag^+ ions. The fundamental mechanism controlling Li-ion transport in porous structures was investigated. Additionally, we developed a unique optimization strategy for tailoring the porosity of m-PSi anodes to enhance battery performance. The electrochemical evaluation revealed that the diffusion coefficient in the PSi quadrupled, reaching 2.347×10^{-9} cm^{-2} s^{-1} from an initial value of 3.68×10^{-10} cm^{-2} s^{-1} as the porosity of m-PSi increased from 4.05 % to 70.01 %. Interestingly, m-PSi-0.06 exhibited the highest diffusion coefficient owing to its optimal mesoporosity. Consequently, it delivered an impressive rate capability of 760 mAh g^{-1} even at a high current density of 4 A g^{-1}, with a recovery rate of 80 %. It also exhibited a high initial capacity of 2914 mAh g^{-1} with 60.9 % retention at a current density of 0.1 A g^{-1} after 100 cycles. These electrochemical results demonstrate that optimal mesoporosity promotes the facile diffusion and efficient charge transfer of Li ions in m-PSi anodes, resulting in enhanced capacity and rate capability. Future research based on these porosity optimization insights could lead to the development of more efficient and durable Si-based anodes with superior kinetics to meet the growing demand for advanced energy storage devices.

2. Experimental Section

2.1. Chemicals used

Si powder (99 % purity, ~5 μm) and hydrofluoric acid solution (HF, 48 %) were obtained from Sigma-Aldrich. Silver nitrate ($AgNO_3$) was acquired from Duksan Pure Chemicals. Nitric acid solution (HNO_3, 70 wt %) and anhydrous ethanol (C_2H_6O, 99.9 %) were obtained from Daejung Chemicals and Metals Co., Ltd., South Korea. All the chemicals were used directly without further purification.

2.2. Preparation of m-Psi anodes

Scheme 1 depicts the widely utilized MACE [23,24] procedure for preparing m-PSi anodes with various porosities. The etchant used was a mixture of $AgNO_3$ (0.06 mol L^{-1}) and 5 M HF in a 1:3 v/v ratio. Initially, 2 g of ~5 μm sized silicon powder was dispersed in 50 mL of deionized (DI) water and stirred continuously at a speed of 250 rpm. Afterward, 200 mL of the etchant solution was slowly poured into the Si dispersion and mixed with stirring for 1 h. Subsequently, the Ag-deposited Si powder precipitated at the bottom of the conical flask. The powder was collected and washed multiple times with DI water to remove unreacted excess etchant solution. To eliminate Ag residues from the m-PSi, the Ag-deposited Si powder was immersed in 200 mL of 70 wt% HNO_3 and stirred for 2 h. After removing Ag, the Si powder was thoroughly washed with DI water and an ethanol solution. Finally, micro-sized porous Si powder (m-PSi-0.06) was obtained as the end-product. The resulting powder was dried overnight in a vacuum oven at 60 °C. The m-PSi synthesized with 0.06 mol L^{-1} $AgNO_3$ in the etchant solution was designated as m-PSi-0.06. Similarly, m-PSi-0.02, m-PSi-0.04, and m-PSi-0.08 samples were prepared using 0.02, 0.04, and 0.08 mol L^{-1} $AgNO_3$, respectively. Furthermore, an electrochemical evaluation was performed, as discussed in **S1.1** of the Supporting Information (**SI**).

3. Results and discussion

According to Scheme 1, the MACE process produces a porous structure in the m-PSi anodic material, as illustrated at the microscopic level. Specifically, five steps are involved in the synthesis of m-PSi, as discussed below.

Step 1: Deposition of Ag on Si:

In the first reaction, the metal catalyst Ag^+ ions are reduced on the Si surface. The Ag^+ ions (from $AgNO_3$) are reduced to Ag metal and deposited as nanoparticles on the Si surface (as shown in Scheme-1(b)) [25].

$$4Ag^+ + 4e^- \rightarrow 4Ag$$

Step 2: Oxidation of Si underneath Ag:

Once the Ag nanoparticles are deposited, they act as a catalyst for the oxidation of Si. The localized oxidation of Si occurs beneath the Ag particles, involving the transfer of electrons from Si to the Ag [26]. The Si atoms below the Ag nanoparticles (AgNPs) lose electrons, leading to the formation of silicon oxide (SiO_2) (Scheme-1 (c)).

$$Si + 2H_2O \rightarrow SiO_2^- + 4H^+ + 4e^-$$

Step 3: Dissolution of silicon dioxide by HF:

Following that, the HF in the solution etch the SiO_2, which was produced in the previous step. HF dissolves the SiO_2 to form soluble $[SiF_6]^{2-}$ ions, exposing more Si for oxidation [23].

$$SiO_2 + 6HF \rightarrow [SiF_6]^{2-} + 2H^+ + 2H_2O$$

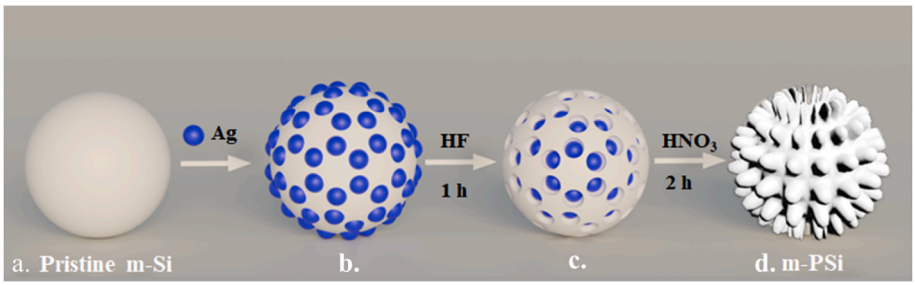

Scheme 1. Schematic of synthesis of micro-sized porous silicon (m-PSi) by MACE process.

Step 4: Continued etching and Ag movement:

After SiO_2 removal, the Ag NPs move deeper into the Si surface, continuing the oxidation process. This movement allows the Ag NPs to etch the Si and create vertical pores, as observed in the Brunauer–Emmett–Teller (BET) analysis [27].

Step 5: Role of HNO_3:

After sufficient etching, HNO_3 converts the embedded Ag NPs in porous Si into $AgNO_3$, which dissolves in water and is subsequently washed away. This process completes the etching, resulting in the formation of m-PSi, as shown in Scheme-1(d). The following reaction occurs during the conversion [28]:

$$3Ag + 4HNO_3 \rightarrow 3AgNO_3 + NO + 2H_2O$$

Similarly, $AgNO_3$ was incorporated into the etchant mixture at various concentrations, ranging from 0.02 to 0.08 mol L^{-1}, to introduce different degrees of porosity in the m-PSi anodes. This approach is based on the assumption that the concentration of Ag^+ ions directly influences the extent of etching, and consequently, the resultant porosity during the MACE process. To systematically investigate the impact of porosity on the D_{Li}^+ and its electrochemical significance for the anode performance, a detailed study was conducted. This included cyclic voltammetry (CV) and electrochemical impedance spectroscopy (EIS) to clarify

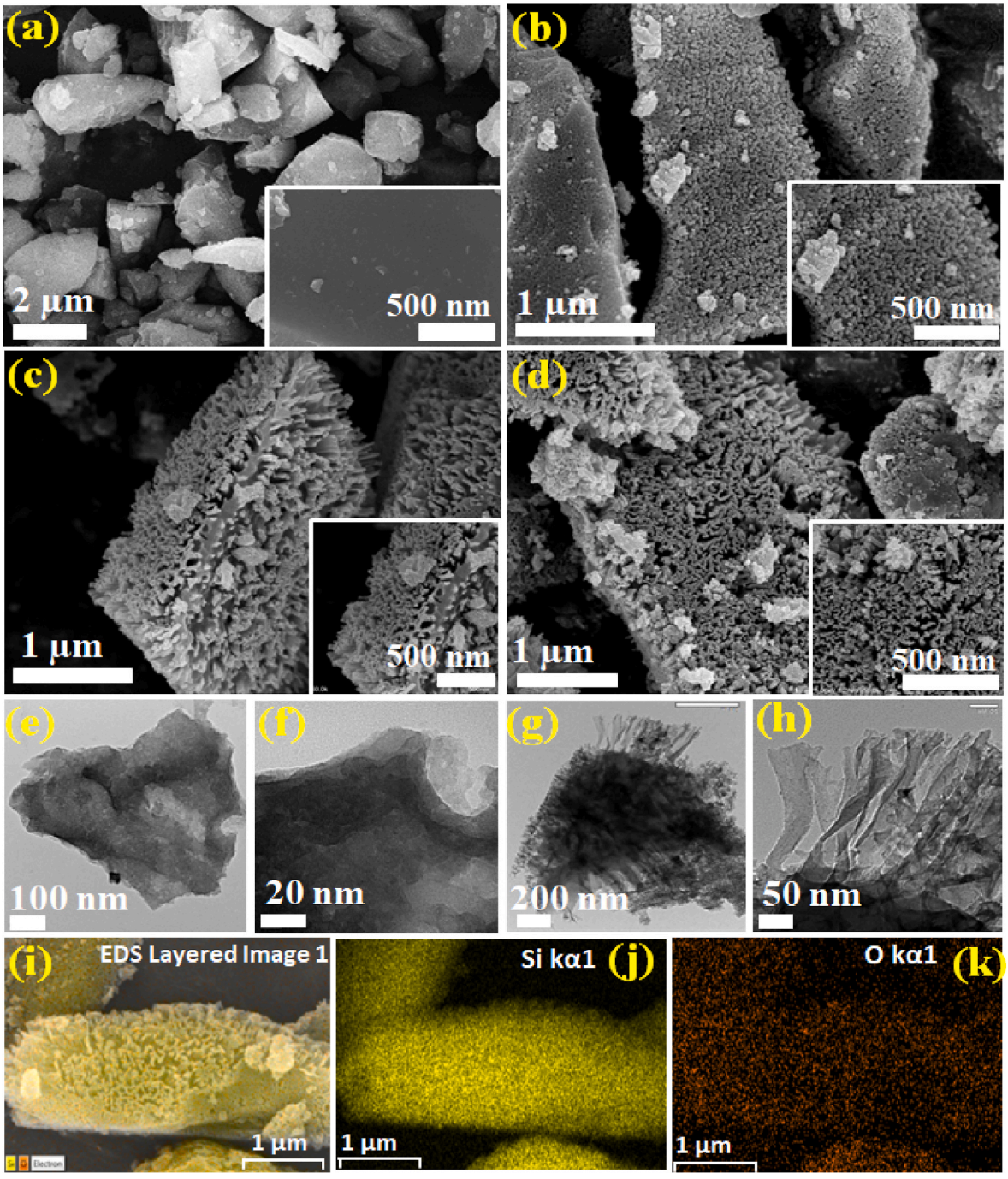

Fig. 1. FE-SEM images of (a) m-Si, (b) m-PSi-0.02, (c) m-PSi-0.04, and (d) m-PSi-0.06. Magnified TEM images of (e–f) m-Si, (g–h) m-PSi-0.06. (i) EDS layered image and elemental mapping of m-PSi-0.06 (j) Si and (k) O.

the complex relationship between porosity and Li-ion diffusion. Furthermore, material characterization is discussed in detail in Section **S1.2** (SI).

3.1. Structural and morphological characterization of as-synthesized samples

Initially, the morphological properties of the m-PSi particles were investigated using field emission-scanning electron microscopy (FE-SEM) analysis. Fig. 1(a) shows the FE-SEM images of m-Si, which shows a pristine polished surface before etching and the inset shows a magnified view of its smooth surface. The m-PSi-0.02 displays a vesicular structure with shallow etching after the MACE process, as shown in Fig. 1(b). In contrast, m-PSi-0.04 exhibits a semi-porous structure due to the finer etching of Si (Fig. 1(c)). Notably, m-PSi-0.06 exhibits a brush-like, highly fibrous porous structure resulting from more effective deep etching, depicted in Fig. 1(d). The magnified image of m-PSi-0.06 showcases a dense array of fibers, indicating that the optimum concentration of the metal catalyst has been achieved. However, m-PSi-0.08 has a spongier porous structure with extremely delicate pores, likely owing to the excessive etching of the porous walls by the concentrated $AgNO_3$ solution (Figs. S1(a and b)). Transmission electron microscopy (TEM) images presented in Fig. 1(e and f) reveal that m-Si maintains a considerably non-porous and bulky structure with a pristine smooth surface. In contrast, Fig. 1(g,h) shows the highly filamentous porous nature of the m-PSi-0.06 after optimized chemical etching. Elemental compositions were evaluated using energy-dispersive X-ray spectroscopy (EDS) mapping (Fig. 1(i–k)), which revealed that m-PSi-0.06 predominantly consists of Si, with trace amounts of oxygen detected, likely attributed to residual oxygen within the m-PSi material [29].

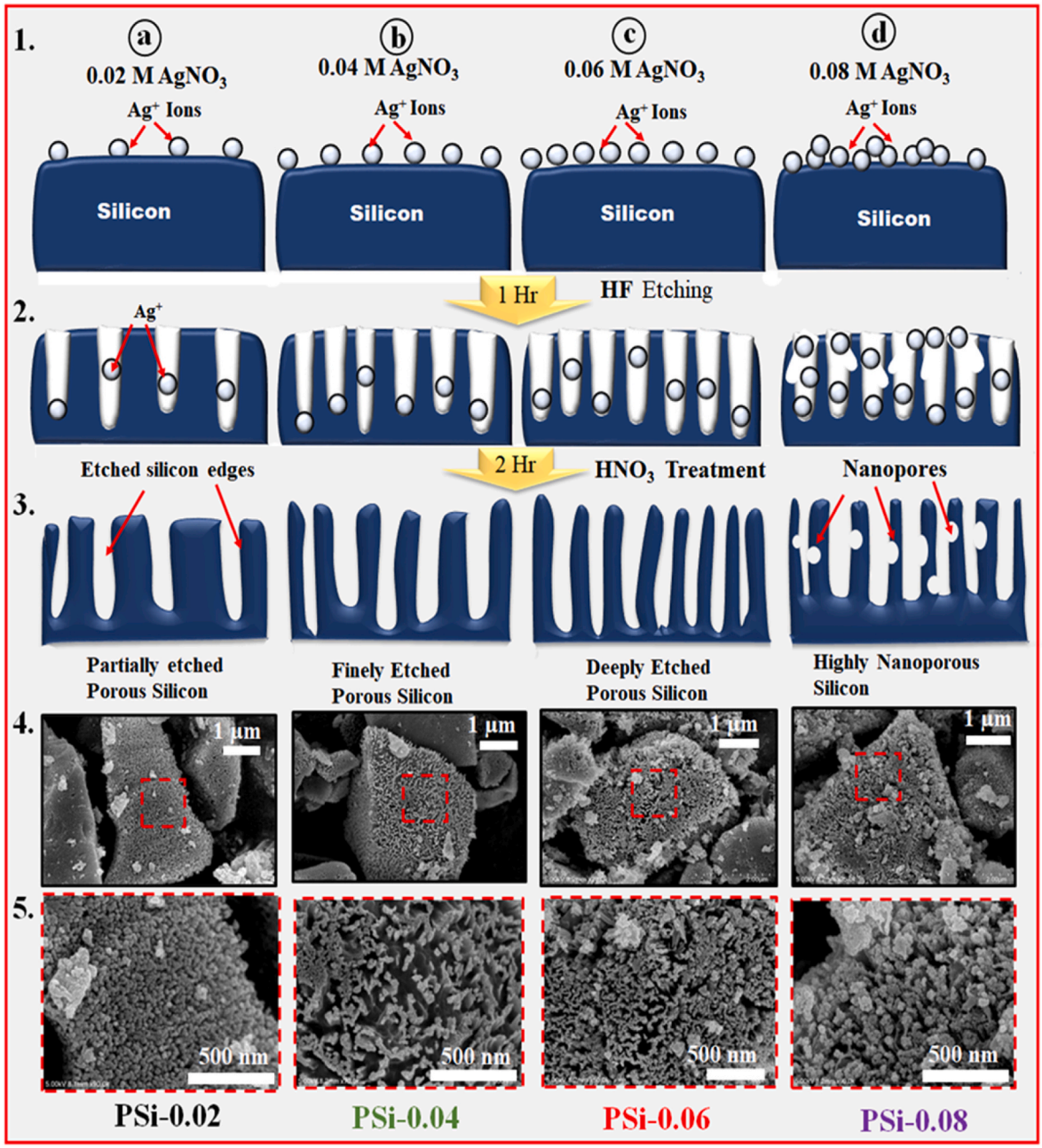

Fig. 2. Schematic illustration depicting the rationale behind varying the concentration of $AgNO_3$ for optimizing the porosity of m-PSi using MACE process.

3.1.1. Rationale for varying $AgNO_3$ concentration for optimizing porosity

Briefly, in the broadest MACE model, the metal catalyst on the Si surface serves as a site for reducing the oxidant [24], specifically the Ag^+ ions derived from $AgNO_3$, as shown in Fig. 2(a–d). Furthermore, the metal catalyst injects a hole (h^+) into the Si interface, while electrons (e^-) are transferred from Si to the catalyst [26]. This process results in a high concentration of holes beneath the Ag^+ ions, creating a hotspot for the oxidation and dissolution of Si after HF treatment, leading to the etching that creates the porous nature of the silicon, as depicted in Fig. 2 (a–d) [30]. The concentration of $AgNO_3$ directly influences the degree of etching and the resulting porosity. It also affects the spatial distribution of etching sites and the subsequent redox reactions beneath the Ag^+ ions, as shown in Scheme 1. To explore this relationship, we used four different concentrations of $AgNO_3$ (0.02, 0.04, 0.06, and 0.08 M) and analyzed the variation in porosity, as shown in Fig. 2(a–d).

According to this relationship, when the concentration of the catalyst is 0.02 M, it fails to cover the entire Si surface effectively, as shown in Fig. 2(a)-2. Consequently, the etching of m-Si occurs at fewer sites, resulting in partially etched and shallow Si surfaces in m-PSi-0.02 (Figs. 2(a)–3). The magnified FE-SEM image of PSi-0.02 shown in Figs. 2 (a)–4, -5, indicates that the resultant sponge-like Si structure exhibits lower porosity and shallower etching. In contrast, at an $AgNO_3$ concentration of 0.04 M, the Ag^+ catalyst covers a larger part of the Si surface, providing more etching sites compared to m-PSi-0.02 (Fig. 2(b)-2). This results in the formation of a more porous brush-like Si structure with 63.2 % porosity, as shown in Figs. 2(b)-4, -5. Further increasing the concentration of $AgNO_3$ to 0.06 M (m-PSi-0.06) allows the catalyst to adequately cover the m-Si surface, facilitating finer and more effective etching to achieve a highly fibrous structure, as depicted in Fig. 2(c)-2, -3. The FE-SEM images in Figs. 2(c)-4, -5 show the dense fibrous structure of m-PSi-0.06 formed after effective etching. However, at a concentration of 0.08 M (m-PSi-0.08), the porosity notably increases to 75.3 % due to a greater number of active etching sites, as shown in Figs. 2(d)–1. The excessive concentration of Ag^+ ions in m-PSi-0.08 causes multilayer deposition on m-Si, leading to irregular etching (Fig. 2 (d)-2). At high concentrations, Ag^+ ions may interfere with one another, restricting effective deep etching. Additionally, the surplus Ag^+ ions can etch the walls of the porous Si channels, generating numerous nanopores, as indicated by the red arrow in Figs. 2(d)–3. This phenomenon is also supported by the intense peak observed at a pore diameter of 1–3 nm in the BET analysis of m-PSi-0.08, which will be discussed later. The FE-SEM image of m-PSi-0.08 shows dimple-shaped and shallowly etched porous Si, as shown in Figs. 2(d)–4. Compared to the other three samples, it exhibits a distinct morphology, as shown in the magnified view of Figs. 2(d)–5. The FE-SEM images of all four m-PSi samples (Fig. 2(a–d)-4) and their subsequent BET data support the hypothesis that varying the concentration of $AgNO_3$ effectively influences the porosity variation (Fig. 4(a–c)).

The crystal structure of the m-Si and m-PSi samples was evaluated using X-ray diffraction (XRD) analysis. All samples exhibit thinner and sharper XRD peaks at distinct 2θ angles, indicating the large and micro-sized nature of the particles, as shown in Fig. 3(a). The peaks observed at 2θ angles of 28.45°, 47.31°, 56.13°, 69.14°, 76.39°, and 88.05° correspond to the (111), (220), (311), (400), (331), and (422) crystallographic planes of cubic-phase pure Si respectively, which is consistent with JCPDS card No. 27–1402 [31,32]. All five samples, including m-Si and m-PSi, exhibited these peaks, confirming that the crystalline nature of silicon was well-preserved throughout the etching process [33]. Additionally, no Ag peaks were observed in the XRD patterns, suggesting that Ag was effectively removed via HNO_3 treatment and subsequent washing [15].

The effect of etching on the chemical compositions of the m-Si and m-PSi samples was further investigated using Fourier-transform infrared (FT-IR) spectroscopy, as shown in Fig. 3(b). All samples exhibited the characteristic Si–Si stretching peak at 600–650 cm^{-1}, indicating the preservation of the crystalline nature of Si throughout the etching

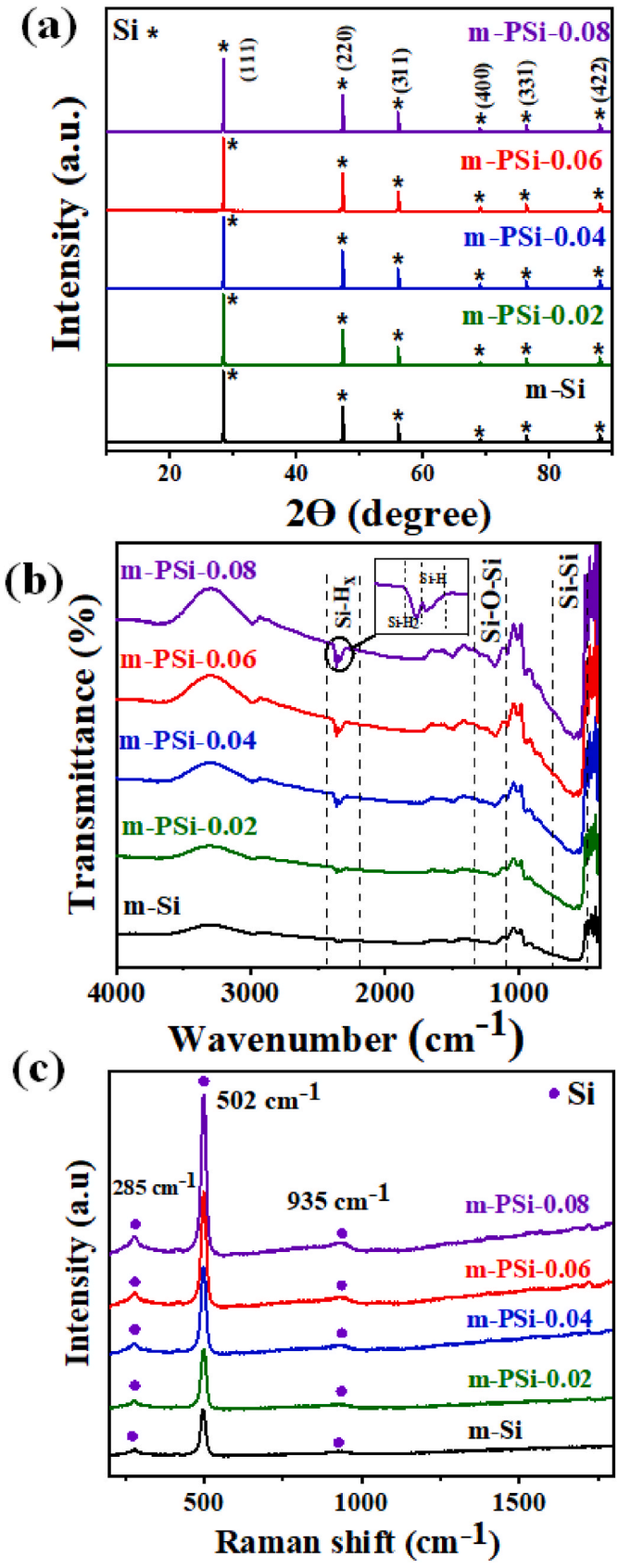

Fig. 3. (a) XRD patterns, (b) FT-IR spectra, and (c) Raman spectra of the m-Si, m-PSi-0.02, m-PSi-0.04, m-PSi-0.06, and m-PSi-0.08 samples.

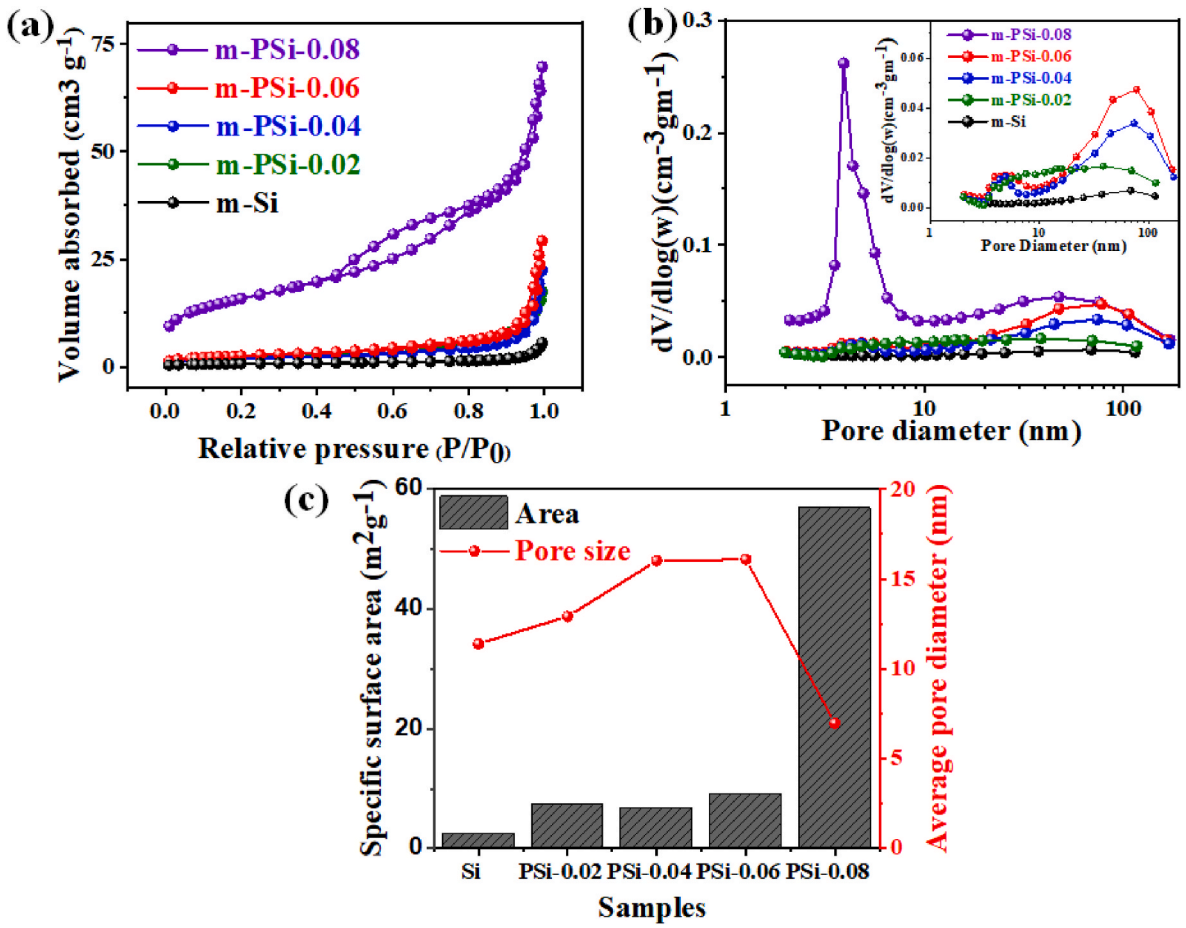

Fig. 4. (a) N_2 absorption/desorption isotherms of the m-Si, m-PSi-0.02, m-PSi-0.04, m-PSi-0.06, and m-PSi-0.08 samples. (b) BJH pore size distribution with an inset showing a comparative analysis excluding m-PSi-0.08. (c) The surface area and pore size of the samples.

process [34]. The presence of a Si–O–Si stretching band at 1180 cm^{-1} indicates occasional oxidation of m-Si due to atmospheric exposure [35, 36]. Moreover, the m-PSi samples displayed sharp doublet peaks at 2140 cm^{-1} and 2160 cm^{-1}, corresponding to Si–H_1 and Si–H_2 species, respectively [36–38]. These bands were absent in the FT-IR spectra of the m-Si sample indicating that they were likely introduced during the formation of m-PSi through the MACE process [26]. The broad band observed around 3600 cm^{-1} is attributed to adsorbed water or hydroxide (–OH) groups resulting from surface oxidation, induced by water residues in the m-PSi samples [39].

Raman spectroscopy was used for the chemical analysis of the m-PSi samples, as shown in Fig. 3(c). Both the m-Si and m-PSi samples exhibit three distinct peaks. The most intense peak at 502 cm^{-1} corresponds to the crystalline phase of Si, attributed to its transverse optical vibrational frequency [40]. The second minor peak at 285 cm^{-1} is associated with SiO_2, whereas the third peak at 935 cm^{-1} is linked to Si–Si stretching in both m-Si and m-PSi samples [41]. Interestingly, varying the concentration of $AgNO_3$ from 0.02 M to 0.08 M during etching does not induce significant chemical changes in the m-PSi samples.

The effect of etching on the fabricated m-PSi samples was further analyzed through BET to evaluate the surface area. The N_2 adsorption/desorption isotherm of the m-PSi samples (Fig. 4(a)) reveals that m-PSi-0.08 has an extensive specific surface area (SSA) (Langmuir = 78.38 m^2 g^{-1}, BET = 56.8 m^2 g^{-1}), which is 6 times larger than that of optimized m-PSi-0.06 (Langmuir = 12.75 m^2 g^{-1}, BET = 9.12 m^2 g^{-1}). Additionally, this surface area is 22 times greater than that of m-Si (Langmuir = 3.52 m^2 g^{-1}, BET = 2.49 m^2 g^{-1}). The improved surface area of the m-PSi samples is attributed to the effective etching of bulk Si via MACE, resulting in a porous structure [42]. As shown in Fig. 4(b), m-PSi-0.08 displays a distinct nanoporous structure with a pore-size range of 1–3 nm, probably owing to excessive etching. In contrast, optimized m-PSi-0.06, m-PSi-0.02, and m-PSi-0.04 exhibit a mesoporous structure with a dual pore-size range distribution ranging from 4 nm to 40–75 nm. Conversely, m-Si exhibits no porosity, as indicated by the flat line in the pore size distribution curve. Fig. 4(c) compares the surface area and pore size of all the m-PSi samples, including m-Si, derived from the BET and BJH analyses. The significant surface area of mPSi-0.08 is due to the formation of nanopores (1–3 nm) within the porous Si walls, as evidenced by the pore size distribution curve as discussed previously. In general, the surface area of the samples increased as the concentration of $AgNO_3$ increased from 0.00 to 0.08 M. The surface area and pore volume distribution values are listed in Table S1. As shown, the mean pore diameter of the sample increases from 11.39 nm (m-Si) to 16.08 nm (m-PSi-0.06) with the rise in $AgNO_3$ concentration. However, when the concentration of $AgNO_3$ reaches its peak value of 0.08 M, the pore size decreases to 6.97 nm. This reduction suggests that at this concentration, extensive etching of m-Si resulted in the formation of extremely small nanopores within the porous walls of m-PSi-0.08, as illustrated in Figs. 2(d)–3. The presence of these nanopores accounts for the highest pore volume of 0.11 cm^{-1} g^{-1}, whereas the optimized m-PSi-0.06 exhibited a pore volume of 0.046 cm^{-1} g^{-1}. Similar to the SSA, the pore volume of both m-Si and m-PSi samples tended to increase with the rising concentration of $AgNO_3$ from 0.00 to 0.08 M, suggesting more effective deep etching of Si with higher $AgNO_3$ concentration.

A mercury powder porosimeter was used to determine the porosities and total pore areas of the synthesized samples, with the results summarized in Table S2. The porosities of m-Si and m-PSi (0.02/0.04/0.06/0.08) samples were found to be 4.05 %, 52.21, 63.20 %, 70.01 %, and

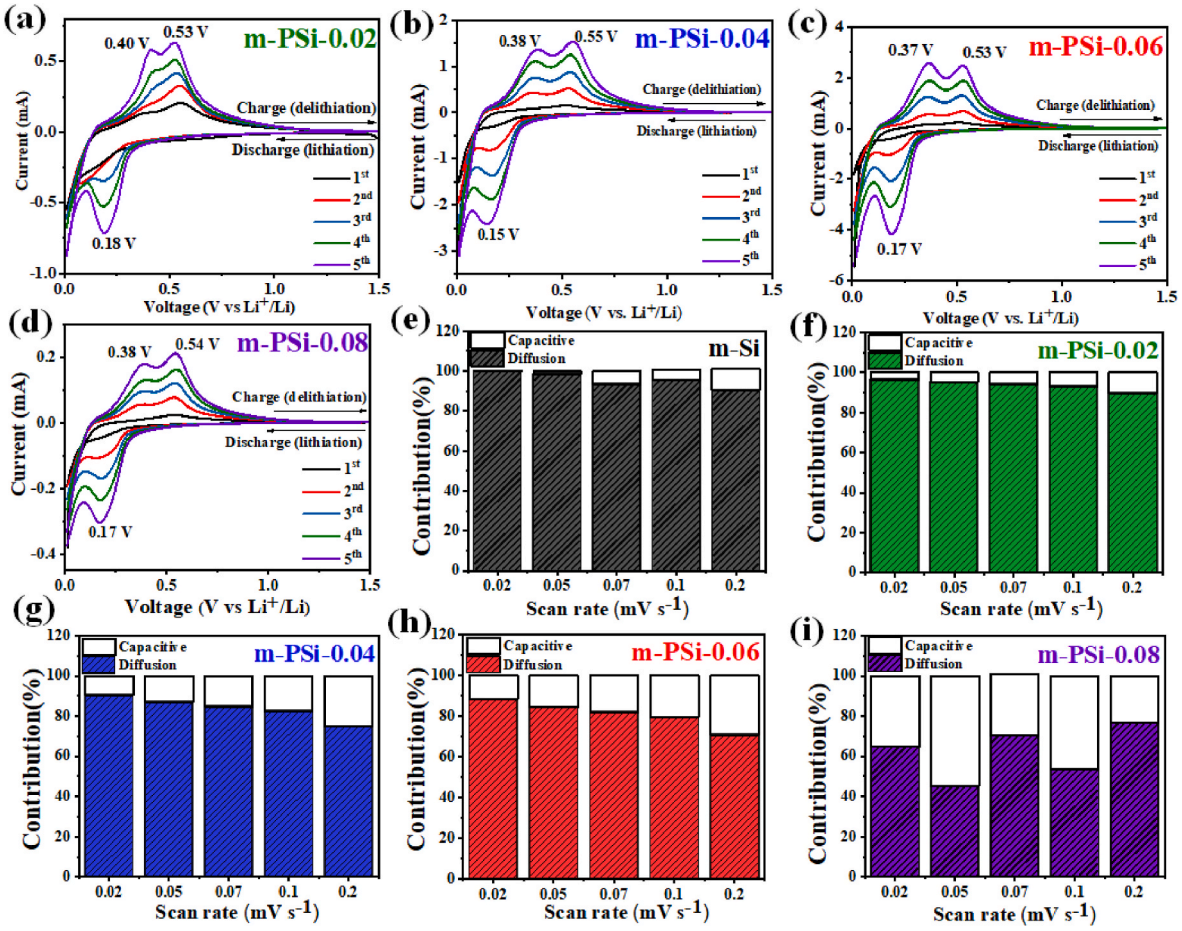

Fig. 5. CV curves for (a) m-PSi-0.02, (b) m-PSi-0.04, (c) m-PSi-0.06, and (d) m-PSi-0.08, recorded over five cycles. Diffusion contributions at various scan rates for (e) m-Si, (f) m-PSi-0.02, (g) m-PSi-0.04 (h) m-PSi-0.06, and (i) m-PSi-0.08, respectively.

75.31 %, respectively. A significant improvement in the porosity of m-PSi has been observed as the concentration of $AgNO_3$ (i.e., Ag^+ metal ion) is gradually increased from 0.02 M to 0.08 M. This finding highlights the crucial role of catalyst concentration in the etching process, demonstrating its positive effect on the porosity of the resultant material. However, at excessive concentrations (m-PSi-0.08) over-etching can occur, leading to a reduction in the average pore volume despite the increase in overall porosity, as previously discussed. The high porosity of m-PSi-0.08 resulted in a notable decrease in material density to 1.98 g/mL, compared to 2.35 g/mL for m-Si. This decrease in density could render the anodes more brittle and susceptible to mechanical failure during repeated charge-discharge cycles. Therefore, optimizing the porosity of m-PSi is essential to maximize its benefits while preserving the structural integrity of the material [43].

3.2. Electrochemical evaluation of the active materials

EIS was conducted before cycling to investigate the reaction kinetics of the m-Si and m-PSi (0.02/0.04/0.06/0.08) electrodes. EIS is a valuable tool for determining the resistance at each kinetic step of an electrochemical reaction, provided that the relevant time constants are accurately identified [44]. The EIS data shown in Fig. S2 shows the evolution of the electrochemical and physical properties during the porosity optimization of the electrodes. In the Nyquist plots (Fig. S2(a)), the resistance R_e represents the electrolyte resistance within the coin cell and contact resistance [45]. The semicircle observed in the high-frequency region, denoted as R_{SEI}, represents the impedance generated by the formation of the SEI layer [46]. The tail in the low-frequency region represents the Warburg impedance (W_s), which is associated with Li-ion diffusion in the Si anodes [47]. The charge transfer resistance at the electrolyte–Si anode interface is denoted as R_{ct} in the EIS plot [48]. The corresponding Nyquist plots and their fitted equivalent circuits are shown in Figs. S2(a and b), with the impedance values summarized in Fig. S2(c). In these circuits, CPE1 and CPE2 represent the constant phase elements, which can be interpreted as capacitances, while WS1 denotes the Warburg constant [49,50]. Interestingly, the cell incorporating optimized m-PSi-0.06 exhibited the lowest R_e value of 1.23 Ω, showing improved redox kinetics. This cell also demonstrated the lowest R_{ct} value of 35.48 Ω, highlighting its efficient charge transfer of Li-ions between the porous Si and electrolyte. This observation shows that the mesoporous channels and pores in m-PSi-0.06 create pathways that facilitate rapid Li-ion transfer. Moreover, the cell with m-PSi-0.06 exhibited a relatively small R_{SEI} value of 55.23 Ω, along with a smaller semicircle in the Nyquist plot, which points to the formation of a stable SEI layer with reduced resistance [51]. In contrast, cells employing m-Si and other m-PSi anodes displayed higher values for all impedance parameters, indicative of poor Li-ion transfer kinetics [52]. Particularly, R_{SEI} values for m-Si and m-PSi (0.02/0.04/0.08) are found to be 157.04 Ω, 107.81 Ω, 98.30 Ω, and 102.5 Ω. Also, R_{ct} values of 71.33 Ω, 64.50 Ω, 42.35 Ω, and 52.23 Ω are obtained for the m-Si and other m-PSi (0.02/0.04/0.08), respectively. This result shows that the m-Si showed the highest R_{SEI} and R_{ct} impedance values, likely due to its dense morphology, which lacks porous channels and limits access to the bulk Si structure. In contrast, m-PSi-0.08 showed higher impedance values than optimized m-PSi-0.06, probably due to its nano porosity, which results in elevated

charge transfer resistance. The irreversible trapping of Li ions in the nanopores may restrict ion diffusion, contributing to higher resistance. Interestingly, the impedance values steadily decreased as the porosity of the micro-sized anodes increased from 4 % in m-Si to 70 % in optimized mPSi-0.06. The enhanced mesoporosity of m-PSi-0.06 significantly improved the diffusion and conduction of Li-ions within the electrode. Although the chemical compositions of the m-Si and m-PSi samples showed no substantial differences, their EIS resistance values varied considerably, underscoring the pivotal role of porosity in governing charge transfer resistance.

The redox behavior of pristine m-Si and m-PSi samples was analyzed using CV within the voltage range of 0.0–1.5 V at a scan rate of 0.2 mV s^{-1}. The resulting voltammograms for m-Si and m-PSi-0.02/0.04/0.06/0.08 samples are depicted in Fig. S3(a) and Fig. 5(a–d). During the initial cathodic reaction, all five samples displayed a prominent peak at around 0.18 V, corresponding to the alloying reactions of crystalline Si with Li-ions, leading to the formation of an amorphous Li_xSi phase [53]. Optimized m-PSi-0.06 exhibited more intense redox peaks (Fig. 5(c)) compared to pristine m-Si (Fig. S3(a)) and m-PSi-0.08 (Fig. 5(d)), indicating improved lithiation facilitated by the optimized mesoporosity [54,55]. During the first anodic process, two dominant peaks appeared at approximately 0.40 V and 0.54 V in the voltammograms of m-PSi samples (Fig. 5(a–d)), which is characteristic of the delithiation of Li_xSi in Si-based anodes [22]. In contrast, the voltammogram of m-Si did not exhibit these distinct delithiation peaks, likely due to the formation of a thick and unstable SEI layer. This increase in SEI resistance is consistent with the EIS data, as shown in Fig. S2(a) [15,56]. Furthermore, the peak positions for both anodic and cathodic reactions remained stable across five lithiation/delithiation cycles for all anode samples, indicating the reversibility of the reaction between Si anodes and Li ions [57]. Notably, the intensity of the redox peaks increased significantly in subsequent cycles, suggesting the progressive activation of the Si electrodes [58]. However, compared to optimized mPSi-0.06, m-PSi-0.08 (Fig. 5(d)) exhibited a significant reduction in peak currents for both anodic and cathodic processes. The weak lithiation–delithiation peaks indicate that the highly nanoporous structure of m-PSi-0.08 impedes the efficient in-out movement of Li ions in and out of the anodes [56]. Conversely, the optimized mesoporous m-PSi-0.06 displayed the highest peak currents in both anodic and cathodic processes, demonstrating a more effective and superior diffusion of Li ions during the cyclic process [19].

The CV at varying scan rates was employed to analyze the effect of porosity on the Li-ion storage mechanism in the m-PSi samples [59]. Fig. S3(b) and Fig. 6(a–d) show the CV profiles of the m-Si and m-PSi (0.02/0.04/0.06/0.08) samples at scan rates in the range of 0.02–0.2 mVs^{-1}. The anodic and cathodic peak currents progressively increased with the rise in scan rate from 0.02 mV s^{-1} to 0.2 mV s^{-1}, indicating the activation of the Si anode surface [60]. Moreover, both peaks shifted to higher and lower potentials due to the elevated polarization of the active m-PSi anodes [54]. The respective plots of peak current versus the square root of the scan rate (i_p Vs. $V^{1/2}$) are shown in Fig. 6(e–h) and Fig. S3(c), while the plots of log i_p Vs. Log $V^{1/2}$ are depicted in Fig. 6(i–l) and Fig. S3(d) for m-PSi samples and m-Si, respectively. The anodic and cathodic kinetics of the active materials are expressed by Eqs. S1 and S2 in **SI (Section S1.3.1)**. Additionally, the interpretation of the slope of log *i vs.* log *v*, i.e., *b*-value, is explained in **SI** (**Section S1.3.2**). Whereas Eqs. S5 and S6 in **SI** (**Section S1.3.3**) were used to calculate the proportional capacitive and diffusion contributions of the m-Si and m-PSi samples by substituting their respective peak current values at various scan rates. Fig. 5(e–i) demonstrates the detailed capacitive contributions for all the active samples at each scan rate. Each sample exhibited a mixed capacitive-diffusion-type Li-ion storage mechanism with varying proportions. Similarly, in the optimized m-PSi-0.06 sample, the capacitive contribution progressively increased with the scan rate, reaching a maximum of approximately 30% at a scan rate of 0.2 mV s^{-1}. The steady increase in the capacitive contribution of m-PSi can be attributed to its controlled mesoporosity, which offers a sufficient number of active sites for Li-ion storage and adsorption reactions [61]. In contrast, m-Si predominantly follows a diffusion-controlled process for Li-ion storage, limiting its capacitive contribution to approximately 10.5 %. The m-PSi-0.08 shows a combination of capacitive and diffusion-controlled

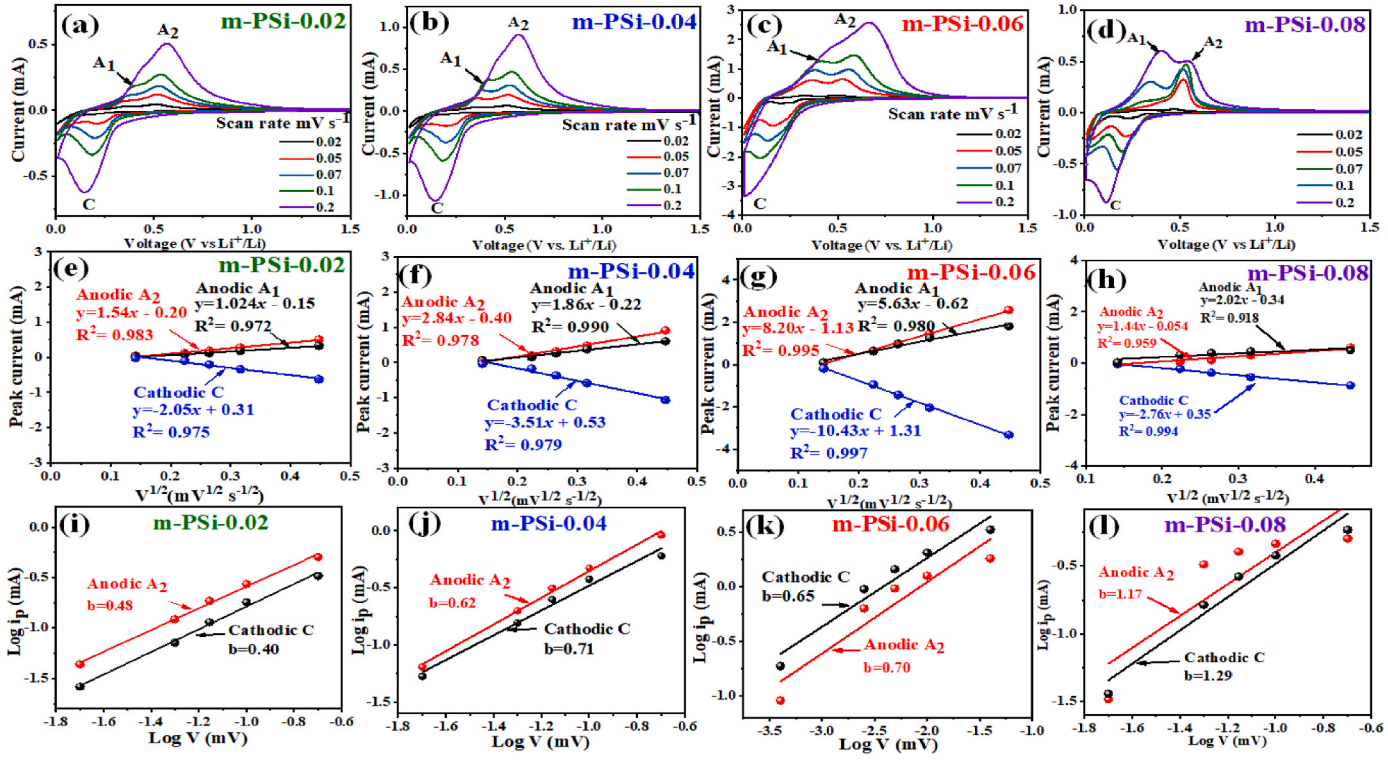

Fig. 6. (a–d) CV curves, (e–h) Plots of peak current density Vs. the square root of scan rate, and (i–l) Logarithmic plots illustrating the relationship between *ip* and *ν* for m-PSi-0.02, m-PSi-0.04, m-PSi-0.06, and m-Psi-0.08 samples.

behaviors but with notable inconsistencies at different scan rates. These inconsistencies are likely due to the introduction of nanopores in m-PSi (Figs. 2(d)–3), which can trap or restrict Li-ion movement, resulting in irregular Li^+ storage performance. In summary, the optimized m-PSi-0.06 sample demonstrates a more consistent mixed capacitive-diffusion mechanism, which tends to shift towards capacitive behavior at a higher scan rate. This behavior is attributed to the efficient adsorption and desorption of Li ions at the electrode-electrolyte interface. The dominant double-layer capacitive behavior of m-PSi-0.06 leads to its superior rate capability, as evidenced by its cyclic performance in Fig. 8(c) [15]. Thus, achieving a balanced combination of capacitive and diffusion-controlled Li-ion storage mechanisms is crucial for enhancing rate capability and cyclic performance [62,63]. The resultant diffusion coefficients of Li-ions were calculated using the Randles–Sevick equation given below [64].

$$I_p = 0.4463 \times AF\left(\frac{F}{RT}\right)^{\frac{1}{2}} C_{Zn^{2+}}\, D_{Li^+}^{\frac{1}{2}} \nu^{\frac{1}{2}} \quad (1)$$

where peak current is given by the I_p, A represents the effective surface area of the anode (1.13 cm^2), F stands for the Faraday constant (96,485 s A mol^{-1}), R gives the gas constant (8.314 J K^{-1} mol^{-1}), T represents the absolute temperature in kelvin, C shows the concentration of Li-ions (1.5 mol cm^{-3}), D_{Li+} is the diffusion coefficient of Li-ions (cm^2 s^{-1}), and υ is the scan rate (mV s^{-1}).

3.3. Impact of porosity on Li-ion diffusion

The calculated D_{Li+} values for each active material are compared graphically in Fig. 7(a). These values were derived from their respective anodic and cathodic peak currents obtained from the CV curves at various scan rates, as illustrated in Fig. 6(a)–(d). Among all samples, m-PSi-0.06 exhibits the highest Li-ion diffusion coefficients of 2.347 × 10^{-9} cm^{-2} s^{-1} and 1.814 × 10^{-9} cm^{-2} s^{-1} for the cathodic and anodic peaks, respectively. This indicates that the optimized m-PSi-0.06 has superior diffusion capabilities. In contrast, the highly nanoporous m-PSi-0.08 sample shows significantly reduced D_{Li+} values of 6.14 × 10^{-10} cm^{-2} s^{-1} and 3.6 × 10^{-10} cm^{-2} s^{-1} for the anodic and cathodic processes, respectively. The other hand, non-porous bulk m-Si shows the poorest Li-ion diffusion, with D_{Li+} values of 3.68 × 10^{-10} cm^{-2} s^{-1} and 1.22 × 10^{-10} cm^{-2} s^{-1} for the cathodic and anodic processes, respectively, due to the absence of porous channels that facilitate ion transport.

Importantly, the influence of the porosity of m-PSi on its Li-ion diffusion is elucidated in Fig. 7(b). As can be observed, m-Si, m-PSi-0.02, m-PSi-0.04, m-PSi-0.06, and m-Psi-0.08 exhibit an anodic D_{Li+} value of 1.22, 3.56, 6.43, 18.14, and 3.56 × 10^{-10} cm^{-2} s^{-1} and the corresponding cathodic D_{Li+} values are 3.68, 4.40, 7.5, 23.47, and 6.14 × 10^{-10} cm^{-2} s^{-1}, respectively. The data clearly indicate that both the anodic and cathodic Li-ion diffusion coefficients of the anodes improve as the porosity increases from 4.05 % (m-Si) to 70.01 % (m-PSi-0.06). However, the coefficients decrease significantly when the porosity reaches its highest value of 75.31 % in m-PSi-0.08. This decline in D_{Li+} for m-PSi-0.08 can be attributed to its highly nanoporous structure with very small pore diameters of 1–3 nm, which may impede the movement of Li ions and even lead to their confinement, thereby limiting their diffusion. In conclusion, mesoporous m-PSi with an optimized mesoporosity of 70.01 % was found to be more beneficial for effective Li-ion diffusion than highly nanoporous structures. This evaluation revealed that varying the porosity effectively influenced the Li-ion diffusion kinetics in the m-PSi anodes.

3.4. Cyclic performance of the as-prepared m-PSi samples

Fig. 8(a) illustrates the cyclic performances of the as-prepared m-PSi samples. The initial discharge capacities of m-Si, m-PSi-0.02, m-PSi-0.04, m-PSi-0.06, and m-PSi-0.08 were 2672, 3131, 3218, 3335, and 3314 mAh g^{-1}, respectively, at the current density of 0.04 A g^{-1}. Additionally, the initial coulombic efficiencies (ICEs) of m-Si, m-PSi-0.02, m-PSi-0.04, m-PSi-0.06, and m-PSi-0.08 samples were calculated as 92.6, 94.0, 96.9, 98.1, and 88.2 %, respectively. Despite the initial loss caused by SEI formation [65], all the tested m-PSi samples achieved an average coulombic efficiency (CE) of 99 % after 10–12 cycles. The average CE values of m-Si and m-PSi-0.06 were 97.2 and 98.6 %, respectively. The capacity retention of the anode materials was calculated using the capacity at the 5^{th} cycle as the initial capacity, assuming the formation of a stable SEI [65]. Among all the samples, m-PSi-0.06 (70.01 % porosity) delivered the highest initial discharge capacity of 3335 mAh g^{-1} and retained 33.5 % of the capacity after 100 cycles, even at a high current density of 0.5 A g^{-1}. In contrast, m-Si, m-PSi-0.02, m-PSi-0.04, and m-PSi-0.08 delivered lower retention rates of 9.3 %, 14.4 %, 14.6 %, and 20.1 %, respectively. The capacity retention improved from m-Si to m-PSi-0.06, as Li-ion diffusion enhanced in the optimized mesoporous Si structures. However, m-PSi-0.08 exhibited a lower retention rate, likely due to reduced Li-ion diffusion resulting from its highly complex nanoporous structure. In addition, its remarkably high surface area can induce side reactions with the electrolyte, potentially impeding its performance [66]. Furthermore, cyclic performance analysis of m-PSi-0.06 at a lower current density of 0.1 A g^{-1} demonstrated an improved capacity retention of 60.9 %, compared to its performance at 0.5 A g^{-1}, as illustrated in Fig. 8(b).

Fig. 8(c) compares the rate capability of the as-prepared m-PSi (0.02/0.04/0.06/0.08) samples in a current density window of 0.1–4.0 A g^{-1}, with capacity evaluations carried out every five cycles. Notably, m-PSi-0.06 delivered high discharge capacities of 3495.02, 2369.01, 1995.51, 1528.31, and 760.48 mAh g^{-1} at current densities of 0.1, 0.2, 1.0, 2.0, and 4.0 A g^{-1}, respectively. Additionally, m-PSi-0.06 showed a promising specific capacity of 2796.02 mAh g^{-1} after 25 cycles with an excellent recovery rate of 80.0 %. In contrast, m-Si, m-PSi-0.02, m-PSi-0.04, and m-PSi-0.08 delivered a poor rate capability of 161.73, 262.72,

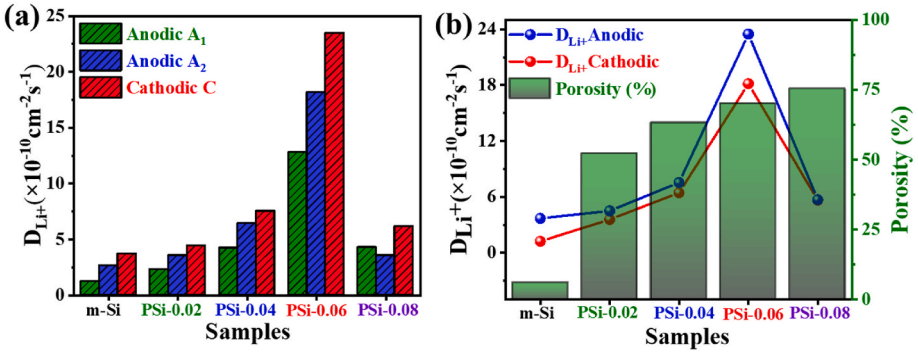

Fig. 7. a) Comparison of D_{Li+} for various active materials, highlighting the differences in diffusion characteristics. b) Relationship between porosity and D_{Li+} for all samples.

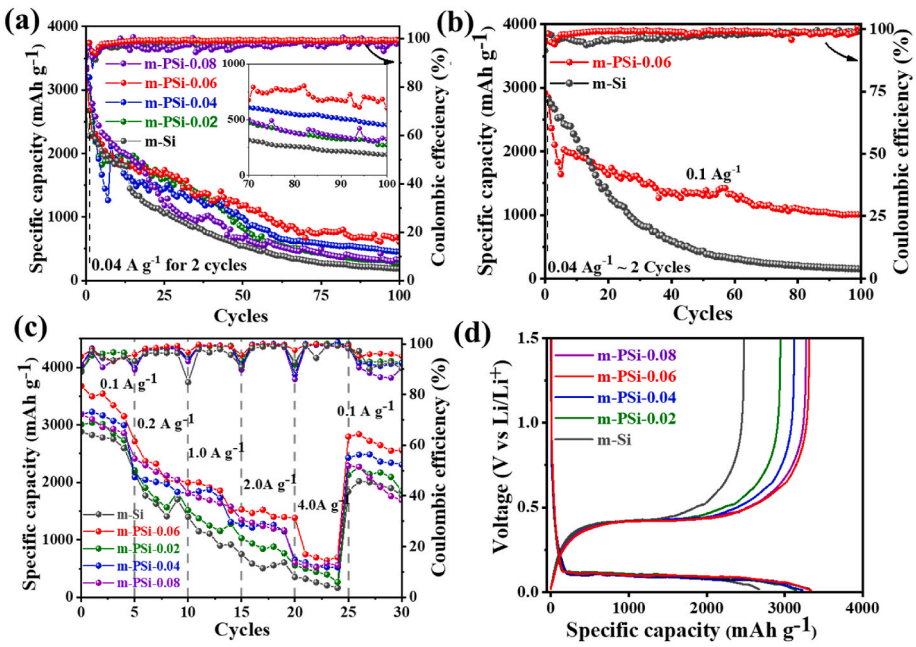

Fig. 8. Cyclic performance of m-Si, m-PSi-0.02, m-PSi-0.04, m-PSi-0.06, and m-PSi-0.08: (a) Performance at a current density of 0.5 A g^{-1}. (b) Cyclic comparison of m-Si and m-PSi-0.06 at a current density of 0.1 A g^{-1}. (c) Rate capability of m-Si, m-PSi-0.02, m-PSi-0.04, m-PSi-0.06 and m-PSi-0.08. (d) Voltage profiles of the initial charge-discharge cycle for all active materials.

521.57, and 558.10 mAh g^{-1} at 4 A g^{-1}, with recovery rates of 65 %, 70 %, 75 %, and 73.8 % after 25 cycles at 0.1 A g^{-1}, respectively. The respective columbic efficiencies of the materials during the rate capability test are depicted in Fig. 8(c). The m-PSi-0.06 sample exhibits an excellent overall efficiency of 97.0 %, whereas m-Si, m-PSi-0.02, m-PSi-0.04, and m-PSi-0.08 exhibit lower efficiencies of 96.8 %, 96.4 %, 95.3 %, and 95.4 %, respectively. Except for m-PSi-0.06, all the materials showed a slight efficiency loss at each interval as the current density increased, indicating the superior stability of the m-PSi-0.06 anodes, even at a high current density of 4 A g^{-1}.

The first charge-discharge cycles of the m-PSi (0.02/0.04/0.06/0.08) and m-Si anodes were analyzed to determine their ICE, as shown in Fig. 8(d). Among the samples, m-PSi-0.06 displays the highest initial discharge capacity of 3335 mAh g^{-1} with a charge capacity of 3268 mAh g^{-1}, resulting in a superior ICE of 98 % at 0.04 A g^{-1}. The minor initial efficiency loss of 2 % was attributed to the irreversible consumption of Li ions in the SEI layer during the charge-discharge cycles. In contrast, m-PSi-0.08 performs poorly with an ICE of 92.1 %, with a charge/discharge capacity of 3052/3314 mAh g^{-1}. The poor efficiency was attributed to the irreversible trapping and restricted movement of Li ions in the highly nanoporous structure of the m-PSi anode, which featured extremely small pore diameters in the range of 1–3 nm. Notably, all the materials achieved an efficiency of approximately 98 % after 10–15 initial cycles.

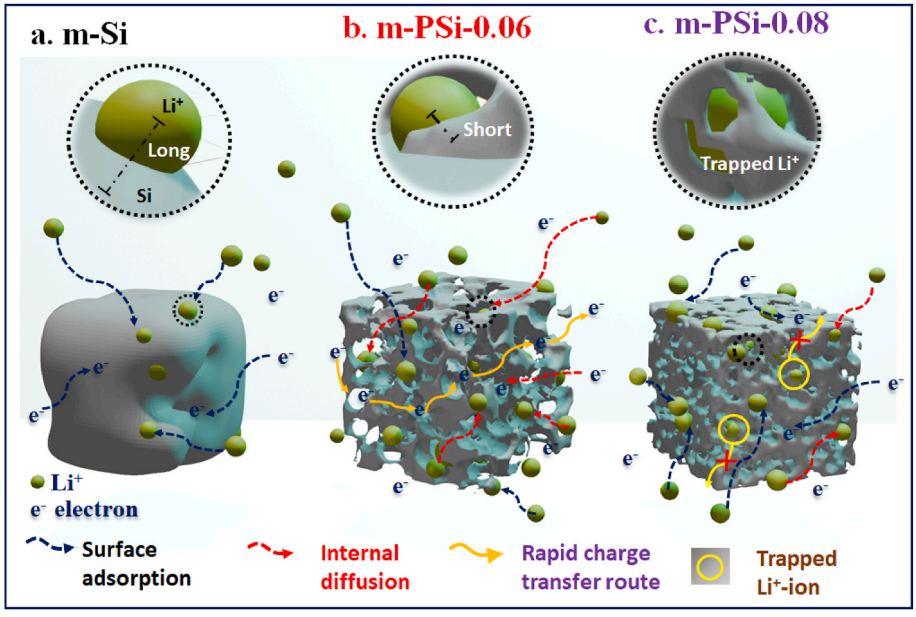

Scheme 2. Proposed mechanism illustrating the enhanced Li-ion diffusion and specific charge transfer processes in pristine m-Si, optimized mesoporous silicon (m-PSi-0.06), and highly nanoporous m-PSi-0.08 anodes during the electrochemical process.

3.5. Mechanism for improved Li^+ diffusion and Interfacial properties

Scheme 2 illustrates the plausible pathways for Li-ion diffusion and electron transmittance in pristine m-Si, optimized m-PSi-0.06, and highly nanoporous m-PSi-0.08 during the electrochemical charge-discharge process. Pristine m-Si, with a negligible porosity of 5 %, exhibits a long diffusion length due to limited access and the absence of directed porous pathways [67]. Consequently, Li-ion storage and electron (e^-) transfer predominantly occur through surface adsorption, as shown in Scheme 2(a) Additionally, the non-porous nature of m-Si leads to extended diffusion paths, as shown in the magnified view in Scheme 2 (a). The lack of facile internal diffusion contributes to a high charge-transfer resistance, as confirmed by the EIS analysis (Fig. S2(a)). In contrast, as shown in Scheme 2(b), the high porosity (70 %) of m-PSi, with its bimodal porous nature (pore diameters ranging from 4 nm to 45–70 nm), facilitates efficient Li-ion diffusion through shorter diffusion pathways within the porous network, as shown in the magnified image within the dotted circle [12]. Li^+ ion diffusion and electron transfer in m-PSi result from a combination of internal diffusion within the mesopores and rapid charge transfer through porous channels [9]. However, as shown in Scheme 2(c), m-PSi-0.08, with a high porosity of 75 % and intricate nanopores (1–3 nm), exhibits a considerably reduced Li^+ diffusion. This reduction is probably because of the irreversible trapping of Li ions in the delicate nanopores, as indicated by the yellow circle in Scheme 2(c) and the magnified view of the black dotted circle, which explains their restricted movement within the tortuous silicon nanostructure. The reduced ICE of 92.1 % indicated the irreversible loss of Li ions in m-PSi-0.08. In conclusion, both the extent and nature of porosity play a crucial role in controlling Li-ion diffusion in m-PSi anodes. While excessive nano porosity can hinder diffusion, an optimized mesoporous structure significantly enhances Li-ion diffusion, thereby improving battery performance, as demonstrated by the m-PSi-0.06 anode.

4. Conclusions

m-PSi samples with varying porosity were synthesized via the MACE process by adjusting the $AgNO_3$ catalyst concentration from 0.02 M to 0.08 M. This approach produced m-PSi samples with porosities of 52.20 %, 63.2 %, 70.01 %, and 75.31 %, corresponding to catalyst concentrations of 0.02 M, 0.04 M, 0.06 M, and 0.08 M, respectively. This systematic optimization approach shows that the m-PSi-0.06 with ~70 % tuned mesoporous nature and a wide pore range (4 nm and 40–70 nm) achieved a superior D_{Li+} of 2.347×10^{-9} cm^{-2} s^{-1}, which is ten times higher than that of m-Si. The m-PSi-0.06 sample demonstrated a notable rate capability of 760 mAh g^{-1} at a high current density of 4 A g^{-1}, with an 80 % recovery rate. Furthermore, it exhibited a high initial capacity of 2914 mAh g^{-1}, retaining 60.9 % of this capacity at a current density of 0.1 A g^{-1}. Kinetic studies conducted via CV and EIS revealed that the extreme nanoporous nature of m-PSi rather restricts the movement of Li-ion movement, whereas its mesoporous nature offers significant benefits for enhanced diffusion and Li-ion storage capabilities. These critical optimization insights can significantly influence the design of highly efficient silicon anodes for advanced LIBs.

CRediT authorship contribution statement

Mahesh B. Naikwade: Writing – original draft, Methodology, Investigation, Formal analysis, Conceptualization. **Pranav K. Katkar:** Writing – review & editing, Validation, Supervision, Formal analysis, Data curation. **Sang-Wha Lee:** Writing – review & editing, Validation, Supervision, Resources, Project administration, Funding acquisition, Conceptualization.

Declaration of competing interest

The authors declare that they have no known competing financial interests or personal relationships that could have appeared to influence the work reported in this paper.

Acknowledgements

This work was supported by the National Research Foundation of Korea (NRF) (NRF-2021R1A6A1A03038996) and the Basic Science Research Capacity Enhancement Project through a Korea Basic Science Institute (National Research Facilities and Equipment Center) (2019R1A6C1010016) grant funded by the Ministry of Science and ICT (MSIT). Additionally, support was provided by the Gachon University Research Fund (GCU-202301050001). We express gratitude for the instrumental analysis at the Smart Materials Research Centre for IoT at Gachon University.

Appendix A. Supplementary data

Supplementary data to this article can be found online at https://doi.org/10.1016/j.ceramint.2024.10.337.

References

[1] L. Sun, Y. Liu, R. Shao, J. Wu, R. Jiang, Z. Jin, Recent progress and future perspective on practical silicon anode-based lithium ion batteries, Energy Storage Mater. 46 (2022) 482–502, https://doi.org/10.1016/j.ensm.2022.01.042.
[2] A. Franco Gonzalez, N.-H. Yang, R.-S. Liu, Silicon anode design for lithium-ion batteries: progress and perspectives, J. Phys. Chem. C 121 (2017) 27775–27787, https://doi.org/10.1021/acs.jpcc.7b07793.
[3] A.N. Singh, M. Islam, A. Meena, M. Faizan, D. Han, C. Bathula, A. Hajibabaei, R. Anand, K.W. Nam, Unleashing the potential of sodium-ion batteries: current state and future directions for sustainable energy storage, Adv. Funct. Mater. 33 (2023) 2304617, https://doi.org/10.1002/adfm.202304617.
[4] K. Feng, M. Li, W. Liu, A.G. Kashkooli, X. Xiao, M. Cai, Z. Chen, Silicon-based anodes for lithium-ion batteries: from fundamentals to practical applications, Small 14 (2018) 1702737, https://doi.org/10.1002/smll.201702737.
[5] Z. Cheng, H. Jiang, X. Zhang, F. Cheng, M. Wu, H. Zhang, Fundamental understanding and facing challenges in structural design of porous Si-based anodes for lithium-ion batteries, Adv. Funct. Mater. 33 (2023) 2301109, https://doi.org/10.1002/adfm.202301109.
[6] A.T.A. Ahmed, R. Soni, A.S. Ansari, C.Y. Lee, H.-S. Kim, H. Im, C. Bathula, Biowaste-derived graphitic carbon interfaced TiO_2 as anode for lithium-ion battery, Surface. Interfac. 35 (2022) 102404, https://doi.org/10.1016/j.surfin.2022.102404.
[7] Z. Yan, J. Jiang, Y. Zhang, D. Yang, N. Du, Scalable and low-cost synthesis of porous silicon nanoparticles as high-performance lithium-ion battery anode, Mater. Today Nano 18 (2022) 100175, https://doi.org/10.1016/j.mtnano.2022.100175.
[8] Y. Liu, L. Qin, F. Liu, Y. Fan, J. Ruan, S. Zhang, Interpenetrated 3D porous silicon as high stable anode material for Li-Ion battery, J. Power Sources 406 (2018) 167–175, https://doi.org/10.1016/j.jpowsour.2018.10.028.
[9] J. Kaspar, M. Graczyk-Zajac, R. Riedel, Determination of the chemical diffusion coefficient of Li-ions in carbon-rich silicon oxycarbide anodes by electro-analytical methods, Electrochim. Acta 115 (2014) 665–670, https://doi.org/10.1016/j.electacta.2013.10.184.
[10] G.A. Tritsaris, K. Zhao, O.U. Okeke, E. Kaxiras, Diffusion of lithium in bulk amorphous silicon: a theoretical study, J. Phys. Chem. C 116 (2012) 22212–22216, https://doi.org/10.1021/jp307221q.
[11] I. Rabani, C. Bathula, R. Zafar, M.S. Shoaib Tahir, Y.-J. Park, H.-S. Kim, M. Naushad, Y.-S. Seo, Visible light-driven photocatalytic rapid degradation of organic contaminants engaging manganese dioxide-incorporated iron oxide three dimensional nanoflowers, J. Colloid Interface Sci. 608 (2022) 2347–2357, https://doi.org/10.1016/j.jcis.2021.10.149.
[12] Y. Luo, L. Huang, J. Liu, Z. Wang, Q. Chen, Y. Chen, The optimization of porosity and particle size for micron-size porous silicon in high energy pre-lithiated silicon–graphite composite for Li-ion batteries, Microporous Mesoporous Mater. 331 (2022) 111672, https://doi.org/10.1002/adma.202005932.
[13] S. Sekar, C. Bathula, I. Rabani, J.W. Lee, S.H. Lee, Y.-S. Seo, S. Lee, Enhanced photocatalytic crystal-violet degradation performances of sonochemically-synthesized AC-CeO_2 nanocomposites, Ultrason. Sonochem. 90 (2022) 106177, https://doi.org/10.1016/j.ultsonch.2022.106177.
[14] M. Ge, J. Rong, X. Fang, C. Zhou, Porous doped silicon nanowires for lithium ion battery anode with long cycle life, Nano Lett. 12 (2012) 2318–2323, https://doi.org/10.1021/nl300206e.
[15] M.B. Naikwade, Y.C. Lee, T.T. Salunkhe, I.T. Kim, T.-A. Nguyen, A. Kadam, S.-W. Lee, Enhanced lithium storage in micro-si-based anode materials through low-temperature interface engineering with an ultrathin phenolic interlayer, ACS Appl. Energy Mater. 7 (2024) 2264–2277, https://doi.org/10.1021/acsaem.3c03002.
[16] Y. Jin, B. Zhu, Z. Lu, N. Liu, J. Zhu, Challenges and recent progress in the development of Si anodes for lithium-ion battery, Adv. Energy Mater. 7 (2017) 1700715, https://doi.org/10.1002/aenm.201700715.

[17] E.-K. Kim, S.J. Yoon, H.T. Bui, S.A. Patil, C. Bathula, N.K. Shrestha, H. Im, S.-H. Han, Epitaxial electrodeposition of single crystal $MoTe_2$ nanorods and Li^+ storage feasibility, J. Electroanal. Chem. 878 (2020) 114672, https://doi.org/10.1016/j.jelechem.2020.114672.

[18] N. Ding, J. Xu, Y.X. Yao, G. Wegner, X. Fang, C.H. Chen, I. Lieberwirth, Determination of the diffusion coefficient of lithium ions in nano-Si, Solid State Ion. 180 (2009) 222–225, https://doi.org/10.1016/j.ssi.2008.12.015.

[19] A.A. Arie, J.K. Lee, A study of Li-ion diffusion kinetics in the fullerene-coated Si anodes of lithium ion batteries, Phys. Scripta T139 (2010) 014013, https://doi.org/10.1088/0031-8949/2010/T139/014013.

[20] B. Long, Y. Zou, Z. Li, Z. Ma, W. Jiang, H. Zou, H. Chen, Effect of phosphorus doping on conductivity, diffusion, and high rate capability in silicon anode for lithium-ion batteries, ACS Appl. Energy Mater. 3 (2020) 5572–5580, https://doi.org/10.1021/acsaem.0c00534.

[21] H. Su, X. Li, C. Liu, Y. Shang, H. Liu, Scalable synthesis of micrometer-sized porous silicon/carbon composites for high-stability lithium-ion battery anodes, Chem. Eng. J. 451 (2023) 138394, https://doi.org/10.1016/j.cej.2022.138394.

[22] Q. Wang, M. Zhu, G. Chen, N. Dudko, Y. Li, H. Liu, L. Shi, G. Wu, D. Zhang, High-performance microsized Si anodes for lithium-ion batteries: insights into the polymer configuration conversion mechanism, Adv. Mater. 34 (2022) 2109658, https://doi.org/10.1002/adma.202109658.

[23] H. Alhmoud, D. Brodoceanu, R. Elnathan, T. Kraus, N.H. Voelcker, A MACEing silicon: towards single-step etching of defined porous nanostructures for biomedicine, Prog. Mater. Sci. 116 (2021) 100636, https://doi.org/10.1016/j.pmatsci.2019.100636.

[24] Z.R. Smith, R.L. Smith, S.D. Collins, Mechanism of nanowire formation in metal assisted chemical etching, Electrochim. Acta 92 (2013) 139–147, https://doi.org/10.1016/j.electacta.2012.12.075.

[25] K. Yamada, M. Yamada, H. Maki, K.M. Itoh, Fabrication of arrays of tapered silicon micro-/nano-pillars by metal-assisted chemical etching and anisotropic wet etching, Nanotech. 29 (2018) 28LT01, https://doi.org/10.1088/1361-6528/aac04b.

[26] Z. Huang, N. Geyer, P. Werner, J. De Boor, U. Gösele, Metal-assisted chemical etching of silicon: a review: in memory of Prof. Ulrich Gösele, Adv. Mater. 23 (2011) 285–308, https://doi.org/10.1002/adma.201001784.

[27] J. Cichoszewski, M. Reuter, F. Schwerdt, J.H. Werner, Role of catalyst concentration on metal assisted chemical etching of silicon, Electrochim. Acta 109 (2013) 333–339, https://doi.org/10.1016/j.electacta.2013.07.079.

[28] D.Z. Dimitrov, C.-H. Du, Crystalline silicon solar cells with micro/nano texture, Appl. Surf. Sci. 266 (2013) 1–4, https://doi.org/10.1016/j.apsusc.2012.10.081.

[29] Y. Gu, Z. He, X. Liu, Y. Sun, S. Jiang, H. Liu, G. Liu, J. Luo, Porous silicon modified wood as a high-efficiency solar steam generator, Eur. J. Wood Wood Prod. 81 (2023) 1177–1188, https://doi.org/10.1007/s00107-023-01952-5.

[30] C. Chartier, S. Bastide, C. Lévy-Clément, Metal-assisted chemical etching of silicon in $HF-H_2O_2$, Electrochim. Acta 53 (2008) 5509–5516, https://doi.org/10.1016/j.electacta.2008.03.009.

[31] J. Zhang, Z. Hou, X. Zhang, L. Zhang, C. Li, Delicate construction of $Si@SiO_x$ composite materials by microwave hydrothermal for lithium-ion battery anodes, Ionics 26 (2020) 69–74, https://doi.org/10.1007/s11581-019-03204-0.

[32] P.A. Sukkurji, I. Issac, S.A. Singaraju, L. Velasco, J.A. Hagmann, W. Bessler, H. Hahn, M. Botros, B. Breitung, Tailored silicon/carbon compounds for printed Li–Ion anodes, Batter. Supercaps 3 (2020) 713–720, https://doi.org/10.1002/batt.202000052.

[33] K. Tamarov, J.D. Swanson, B.A. Unger, K.W. Kolasinski, A.T. Ernst, M. Aindow, V.-P. Lehto, J. Riikonen, Controlling the nature of etched Si nanostructures: high-versus low-load metal-assisted catalytic etching (MACE) of Si powders, ACS Appl. Mater. Interfaces 12 (2020) 4787–4796, https://doi.org/10.1021/acsami.9b20514.

[34] T. Jutarosaga, J.S. Jeoung, S. Seraphin, Infrared spectroscopy of Si–O bonding in low-dose low-energy separation by implanted oxygen materials, Thin Solid Films 476 (2005) 303–311, https://doi.org/10.1016/j.tsf.2004.10.006.

[35] E.S. San Andrés, A. Del Prado, I. Mártil, G. González-Dıaz, D. Bravo, F.J. López, M. Fernández, W. Bohne, J. Röhrich, B. Selle, I. Sieber, Bonding configuration and density of defects of SiO_xH_y thin films deposited by the electron cyclotron resonance plasma method, J. Appl. Phys. 94 (2003) 7462–7469, https://doi.org/10.1063/1.1626798.

[36] Y.H. Ogata, Characterization of Porous Silicon by Infrared Spectroscopy, Handbook of Porous Silicon, Springer, 2014, pp. 473–480.

[37] T. Kaneko, D. Nemoto, A. Horiguchi, N. Miyakawa, FTIR analysis of a-SiC: H films grown by plasma enhanced CVD, J. Cryst. Growth 275 (2005) e1097–e1101, https://doi.org/10.1016/j.jcrysgro.2004.11.128.

[38] J. Wang, J. Joo, R.M. Kennard, S.-W. Lee, M.J. Sailor, Thermolytic grafting of polystyrene to porous silicon, Chem. Mater. 28 (2016) 79–89, https://doi.org/10.1021/acs.chemmater.5b03221.

[39] E. Herth, R. Zeggari, J.-Y. Rauch, F. Remy-Martin, W. Boireau, Investigation of amorphous SiOx layer on gold surface for surface plasmon resonance measurements, Microelectron. Eng. 163 (2016) 43–48, https://doi.org/10.1016/j.mee.2016.04.014.

[40] Y. Zhao, D. Li, D. Yang, Al-assisted anodic etched porous silicon, J. Mater. Sci. 41 (2006) 5283–5286, https://doi.org/10.1007/s10853-006-0267-5.

[41] M.X. Tran, J.-Y. Woo, T.-A. Nguyen, S.-W. Lee, J.K. Lee, Thermolytically grafted silicon particles with ultrathin carbonaceous coating rich of phenyl moieties as lithium-storage anode material, Chem. Eng. J. 395 (2020) 125169, https://doi.org/10.1016/j.cej.2020.125169.

[42] R.P. Srivastava, D.Y. Khang, Structuring of Si into multiple scales by metal-assisted chemical etching, Adv. Mater. 33 (2021) e2005932, https://doi.org/10.1002/adma.202005932.

[43] J. Sun, J. Li, B. Ban, J. Shi, Q. Wang, J. Chen, A simple method to fabricate size and porosity tunable Si by Al–Si alloy as lithium ion battery anode material, Electrochim. Acta 345 (2020) 136242, https://doi.org/10.1016/j.electacta.2020.136242.

[44] J. Guo, A. Sun, X. Chen, C. Wang, A. Manivannan, Cyclability study of silicon–carbon composite anodes for lithium-ion batteries using electrochemical impedance spectroscopy, Electrochim. Acta 56 (2011) 3981–3987, https://doi.org/10.1016/j.electacta.2011.02.014.

[45] L. Wen, L. Wang, Z. Guan, X. Liu, M. Wei, D. Jiang, S. Zhang, Effect of composite conductive agent on internal resistance and performance of lithium iron phosphate batteries, Ionics 28 (2022) 3145–3153, https://doi.org/10.1007/s11581-022-04491-w.

[46] D.A. Lozhkina, A.M. Rumyantsev, E.V. Astrova, Impedance spectroscopy of porous silicon and silicon-carbon anodes produced by sintering, Semiconductors 54 (2020) 383–391, https://doi.org/10.1134/S1063782620030124.

[47] Y.-S. Lee, K.-S. Ryu, Study of the lithium diffusion properties and high rate performance of $TiNb_6O_{17}$ as an anode in lithium secondary battery, Sci. Rep. 7 (2017) 16617, https://doi.org/10.1038/s41598-017-16711-9.

[48] H. Zhang, X. Qin, J. Wu, Y.-B. He, H. Du, B. Li, F. Kang, Electrospun core–shell silicon/carbon fibers with an internal honeycomb-like conductive carbon framework as an anode for lithium ion batteries, J. Mater. Chem. A 3 (2015) 7112–7120, https://doi.org/10.1039/C4TA06044J.

[49] T.L. Kulova, Y.V. Pleskov, A.M. Skundin, E.I. Terukov, O.I. Kon'kov, Lithium intercalation into amorphous-silicon thin films: an electrochemical-impedance study, Russ. J. Electrochem. 42 (2006) 708–714, https://doi.org/10.1134/S1023193506070032.

[50] Y. Yamada, Y. Iriyama, T. Abe, Z. Ogumi, Kinetics of electrochemical insertion and extraction of lithium ion at SiO, J. Electrochem. Soc. 157 (2010) A26, https://doi.org/10.1149/1.3247598.

[51] M. Su, S. Liu, H. Wan, A. Dou, K. Liu, Y. Liu, Effect of binders on performance of Si/C composite as anode for Li-ion batteries, Ionics 25 (2019) 2103–2109, https://doi.org/10.1007/s11581-018-2611-6.

[52] K. Pan, F. Zou, M. Canova, Y. Zhu, J.-H. Kim, Comprehensive electrochemical impedance spectroscopy study of Si-Based anodes using distribution of relaxation times analysis, J. Power Sources 479 (2020) 229083, https://doi.org/10.1016/j.jpowsour.2020.229083.

[53] B. Jerliu, E. Hüger, L. Dörrer, B.K. Seidlhofer, R. Steitz, M. Horisberger, H. Schmidt, Lithium insertion into silicon electrodes studied by cyclic voltammetry and operando neutron reflectometry, Phys. Chem. Chem. Phys. 20 (2018) 23480–23491, https://doi.org/10.1039/C8CP03540G.

[54] M. Choi, J.-C. Kim, D.-W. Kim, Waste windshield-derived silicon/carbon nanocomposites as high-performance lithium-ion battery anodes, Sci. Rep. 8 (2018) 960, https://doi.org/10.1038/s41598-018-19529-1.

[55] W. Wang, Z. Favors, R. Ionescu, R. Ye, H.H. Bay, M. Ozkan, C.S. Ozkan, Monodisperse porous silicon spheres as anode materials for lithium ion batteries, Sci. Rep. 5 (2015) 8781, https://doi.org/10.1038/srep08781.

[56] S. Yin, Q. Ji, X. Zuo, S. Xie, K. Fang, Y. Xia, J. Li, B. Qiu, M. Wang, J. Ban, X. Wang, Y. Zhang, Y. Xiao, L. Zheng, S. Liang, Z. Liu, C. Wang, Y.J. Cheng, Silicon lithium-ion battery anode with enhanced performance: multiple effects of silver nanoparticles, J. Mater. Sci. Technol. 34 (2018) 1902–1911, https://doi.org/10.1016/j.jmst.2018.02.004.

[57] Z. Zhang, H. Ying, P. Huang, S. Zhang, Z. Zhang, T. Yang, W.-Q. Han, Porous Si decorated on MXene as free-standing anodes for lithium-ion batteries with enhanced diffusion properties and mechanical stability, Chem. Eng. J. 451 (2023) 138785, https://doi.org/10.1016/j.cej.2022.138785.

[58] K.W. Schroder, H. Celio, L.J. Webb, K.J. Stevenson, Examining solid electrolyte interphase formation on crystalline silicon electrodes: influence of electrochemical preparation and ambient exposure conditions, J. Phys. Chem. C 116 (2012) 19737–19747, https://doi.org/10.1021/jp307372m.

[59] R. Kumar, M. Bag, Quantifying capacitive and diffusion-controlled charge storage from 3D bulk to 2D layered halide perovskite-based porous electrodes for efficient supercapacitor applications, J. Phys. Chem. C 125 (2021) 16946–16954, https://doi.org/10.1021/acs.jpcc.1c05493.

[60] A. Paravannoor, D. Panoth, P. Pattathil, Silicon anode design for Li ion batteries: synergic effects of Ag nanoparticles and ionic liquid electrolytes, Eng. J. 4 (2020) 100037, https://doi.org/10.1016/j.ceja.2020.100037.

[61] Y. Tang, J. Chen, Z. Mao, C. Roth, D. Wang, Highly N-doped carbon with low graphitic-N content as anode material for enhanced initial Coulombic efficiency of lithium-ion batteries, Carbon Energy 5 (2023) e257, https://doi.org/10.1002/cey2.257.

[62] M.X. Tran, T.-A. Nguyen, J.K. Lee, S.-W. Lee, Porous silicon covalently-grafted with chloro-styrenic carbons for fast Li^+ diffusion and durable lithium-storage capability, J. Power Sources 554 (2023) 232326, https://doi.org/10.1016/j.jpowsour.2022.232326.

[63] P.K. Katkar, M.B. Naikwade, S.A. Patil, S.-W. Lee, Self-assembly of $Sr_2P_2O_7$@ 2D rGO nano/micro-architecture for highly durable and bendable solid-state supercapattery, Mater. Today Phys. 46 (2024) 101510, https://doi.org/10.1016/j.mtphys.2024.101510.

[64] F. Zhang, J. Yang, Boosting initial coulombic efficiency of Si-based anodes: a review, Materials 3 (2020) 369–380, https://doi.org/10.1007/s42247-020-00080-7.

[65] T. Shen, Z. Yao, X. Xia, X. Wang, C. Gu, J. Tu, Rationally designed silicon nanostructures as anode material for lithium-ion batteries, Adv. Eng. Mater. 20 (2018) 1700591, https://doi.org/10.1002/adem.201700591.
[66] S. Chen, Z. Chen, X. Xu, C. Cao, M. Xia, Y. Luo, Scalable 2D mesoporous silicon nanosheets for high-performance lithium-ion battery anode, Small 14 (2018) e1703361, https://doi.org/10.1002/smll.201703361.
[67] J. Li, J. Huang, J. Li, L. Cao, H. Qi, Y. Cheng, Q. Xi, H. Dang, Improved Li-ion diffusion process in TiO_2/rGO anode for lithium-ion battery, J. Alloys Compd. 727 (2017) 998–1005, https://doi.org/10.1016/j.jallcom.2017.08.121.